The Effect of Ultrasonic Melt Treatment on Macro-Segregation and Peritectic Transformation in an Al-19Si-4Fe Alloy

C.J. TODARO, M.A. EASTON, D. QIU, G. WANG, D.H. STJOHN, and M. QIAN

It is well documented that ultrasonic melt treatment (USMT) can refine dendritic and eutectic microstructures during solidification, but much less attention has been paid to the effect of USMT on macro-segregation and intermetallic transformations. In this research, macro-segregation and primary Fe-containing intermetallic peritectic transformations in an Al-19 wt pct Si-4 wt pct Fe alloy were investigated without and with USMT. Macrostructural examination showed that in the absence of USMT the ingot revealed considerable non-uniform distribution of both the primary Fe-containing intermetallic and primary Si particles, whereas the ingot with USMT exhibited near homogeneous distribution of both primary phases, *i.e.,* reduced macro-segregation. The beneficial effect of USMT on relieving macro-segregation was further examined using quantitative microstructural metallography and the results indicated that the area fraction, number density, and size distribution of both primary phases became essentially uniform across the ingot after USMT. USMT further exerted a significant impact on the constitution of the primary Fe-containing intermetallics, where complex particles of δ-Al_3FeSi_2/β-Al_5FeSi were prominent without USMT, while few δ-Al_3FeSi_2 particles were observed after USMT and the primary Fe-containing intermetallics existed mostly as the single-phase β-Al_5FeSi. The underlying reason was attributed to the reduction in the size of the primary δ-Al_3FeSi_2 particles which ensures the complete transformation of most primary δ-Al_3FeSi_2 particles to the peritectic β-Al_5FeSi phase.

DOI: 10.1007/s11661-017-4325-1
© The Minerals, Metals & Materials Society and ASM International 2017

I. INTRODUCTION

AL-SI based alloys are the most widely used Al-based foundry alloys due to their excellent combination of mechanical properties and ease of castability. Hypoeutectic Al-Si alloys containing 5 to 12 wt pct Si (wt pct is used hereinafter unless otherwise specified) account for most commercial production. However, hypereutectic Al-Si alloys with 14 to 25 pct Si are more desirable for applications requiring wear resistance, along with high strength and low weight. Transition metal solutes, notably Fe, Cr, and Ni, in these alloys can further improve their performance at elevated temperatures due to the presence of thermally stable intermetallics.[1,2] The use of Fe is considered to be particularly attractive for two reasons: it alleviates die soldering for die casting and allows the use of secondary Al (post-consumer scrap) already containing appreciable amounts of Fe. However, the amount of Fe addition is restricted as the resulting Fe-containing intermetallics can form as large and coarse platelet-like features, deteriorating ductility and fracture toughness.[3] Moreover, it is challenging to obtain microstructurally homogeneous castings of hypereutectic Al-Si-based alloys by conventional foundry processes, because of the propensity to form macro-segregation defects during solidification.[4] As a result, special solidification processes such as rapid solidification,[5] spray deposition,[6] melt thermal-rate treatment (MTRT),[7] and ultrasonic melt treatment (USMT)[8–13] have been employed to control the size, morphology, and distribution of Fe-containing intermetallics and primary Si in hypereutectic Al-Si alloys.

In Fe-containing hypereutectic Al-Si alloys, the Al-Fe-Si phase diagram[14] shows that the following three reactions can occur leading to the formation of β-Al_5FeSi during equilibrium solidification:

(1) $L + \delta\text{-}Al_3FeSi_2 \rightarrow \beta\text{-}Al_5FeSi + Si$
(2) $L \rightarrow \beta\text{-}Al_5FeSi + Si$

C.J. TODARO, M.A. EASTON, M. QIAN, and D. QIU are with the Centre for Additive Manufacturing, School of Engineering, RMIT University, Melbourne, VIC 3000, Australia. Contact e-mail: ma.qian@rmit.edu.au D.H. StJOHN and G. WANG are with the Centre for Advanced Materials Processing and Manufacturing (AMPAM), School of Mechanical and Mining Engineering, The University of Queensland, St Lucia, QLD 4072, Australia.
Manuscript submitted April 17, 2017.
Article published online September 18, 2017

Table I. Previous Studies on USMT of Hypereutectic Al-Si Based Alloys Containing Deliberate Additions of Fe

Si, Fe Content (Pct)	Neutralizing Elements (Pct)	Primary Phase	Macro-Segregation Reported	Influence on Peritectic Solidification: Suppression	Influence on Peritectic Solidification: Promotion	Horn Material	Horn Diameter (mm)	Applied Power (W)	Amplitude (μm)	Frequency (kHz)	Horn Temp. (K)	Horn Immersion Depth (mm)	Melt Size (g)	Pouring Temp.* (K)	Difference in	References
17, 1.3	Mn = 0.5	Si	no	phases not characterized		stainless steel	crucible-type	2000	25 to 30	19.5	room temp.	N/A	1300	no difference		13
17, 2	Mn = 0.8	Si	no	no effect		Ti	*NS*	1600	*NS*	20	*NS*	15 to 20	600	85 to 125		11
17, 2	Mn = 0.4, 0.8	Si	no	β-phase	δ-phase	Ti	*NS*	1600	*NS*	20	*NS*	15 to 20	600	110		12
18, 4	none	δ-phase	no	no effect		Sialon	20	1200	20	19	*NS*	10	240	Not poured		8
20, 0.7	Co = 0 to 1.5	Si	no	no effect		Ti	*NS*	1200	*NS*	20	*NS*	15 to 20	600	135		10
20, 2	Mn = 0.0, 0.5	Si	no	β-phase	δ-phase	Ti	*NS*	1200	*NS*	20	*NS*	15 to 20	600	130		9

Note: The difference in pouring temperature refers to the difference in pouring temperature used without and with USMT.
NS.: not specified.

(3) $L \rightarrow \alpha\text{-Al} + \text{Si} + \beta\text{-Al}_5\text{FeSi}$.

During reaction (1), the β-Al_5FeSi phase forms on δ-Al_3FeSi_2 *via* a quasi-peritectic reaction which occurs only when the Si and Fe contents are greater than ~17.7 and ~2.8 pct, respectively, by thermodynamic calculations using the software package Pandat™ and PanAluminium 2016 database. When the Si and Fe solute concentrations are more dilute, however, the β-Al_5FeSi phase can simply form directly from the liquid as a pre-eutectic phase according to reaction (2). Finally, some β-Al_5FeSi phase can form as a component of the α-Al + Si + β-Al_5FeSi ternary eutectic by reaction (3). Nonetheless, the phase δ-Al_3FeSi_2 has been reported to also exist in dilute Al-Fe-Si alloys,[15] highlighting the complexity of the Al-Fe-Si system. Furthermore, peritectic β-Al_5FeSi often coexists with the primary δ-Al_3FeSi_2 phase in the as-cast microstructure, because the peritectic transformation of δ-Al_3FeSi_2 into β-Al_5FeSi in reaction (1) rarely goes to completion. Two studies have investigated quasi-peritectic reactions in the Al-Fe-Si system,[16,17] but they both dealt with low Fe hypoeutectic Al-Si alloys. Hence, there is a lack of understanding of the solidification reactions that occur in hypereutectic Al-Si alloys containing moderate additions of Fe and the growth mechanisms involved.

USMT has been employed in solidification processing to control the nucleation and growth of primary crystalline phases, together with the macro- and microstructural features in castings.[18–26] Hence, the use of USMT has attracted attention for refining the size and modifying the morphology of Fe-containing intermetallics[8,27] and primary Si,[28–30] including when both phases coexist in hypereutectic Al-Si alloys.[8–13] Table I summarizes the studies on USMT of hypereutectic Al-Si alloys containing deliberate additions of Fe. However, in these reports, inadequate information was provided on the experimental parameters, such as the ultrasonic horn diameter, ultrasonic amplitude, and horn pre-heating temperature, which makes it difficult to compare the results. Furthermore, very different melt temperatures or superheats were used (Table I), which are known to have an important effect on the microstructure, *e.g.,* the use of a lower melt temperature tends to produce a finer grain structure.[31] Therefore, it is important to isolate the effect of the melt temperature from that of USMT.

Previous studies[9,12] have shown that USMT suppresses the formation of the peritectic β-phase in hypereutectic Al-Si based alloys, but leads to the formation of the primary δ-phase instead. This implies that USMT can stifle the peritectic transformation δ-$Al_3FeSi_2 \rightarrow \beta$-$Al_5FeSi$. However, contrasting results have also been reported on other alloy systems such as Sb-Sn,[32] Cu-Sn,[33] and Ti-Al,[34] in which peritectic transformations were clearly promoted by USMT. This difference demands an in-depth investigation into the role of USMT on the peritectic transformation of primary Fe-containing intermetallics in hypereutectic Al-Si alloys. Additionally, although USMT has been shown to be effective in mitigating separation in immiscible Al-Sn-Cu alloys,[35,36] no systematic study

has been presented yet on the effect of USMT on macro-segregation in conventional Al alloys.

In view of this, this study was carried out to evaluate the macro-segregation and the formation of Fe-containing intermetallics in a slowly cooled Al-19Si-4Fe alloy without and with USMT. The ternary alloying addition of 4 pct Fe was selected because (i) it ensures the occurrence of the quasi-peritectic reaction L + δ-Al_3FeSi_2 → β-Al_5FeSi + Si; (ii) it produces a sufficient volume fraction of intermetallic phases facilitating microscopic investigation; and (iii) it is comparable to the additions of Fe in previous studies (see Table I).

II. EXPERIMENTAL PROCEDURES

A. *Materials*

The Al-19Si-4Fe alloy was produced by melting commercially pure Al (99.7 pct), Si (99.5 pct), and an Al-10Fe master alloy at 1073 K (800 °C) in an induction furnace and held for 10 minutes before casting into boron nitride-coated steel molds to produce 350 g ingot charges. A single ingot charge was then placed in a boron nitride-coated clay-graphite crucible (90 mm top outer diameter, 55 mm bottom outer diameter, and 92 mm in height) and remelted and held in a resistance furnace at 1073 K (800 °C) for 30 minutes. The liquid alloy was stirred for 1 minute for complete and homogeneous dissolution and then furnace-cooled. The melt temperature was recorded with a frequency of 10 readings per second by a K-type thermocouple located approximately one-half radius from the inner crucible wall. The first derivative cooling curves were mathematically smoothed using the adjacent-average method over 25 data points (no further smoothing was applied). The cooling rate prior to primary phase formation was ~0.15 K s^{-1}.

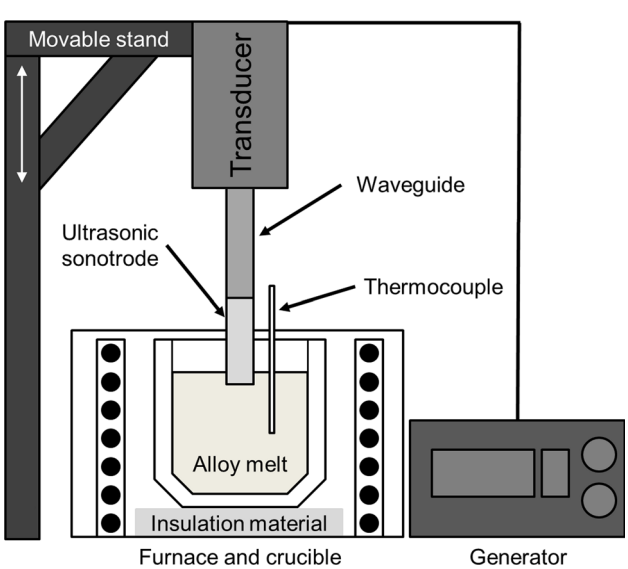

Fig. 1—Schematic illustration of the experimental set-up.

B. *USMT Procedure*

Figure 1 displays the USMT set-up. The commercial ultrasonic system comprises a 500-W generator, a fan-cooled 20 kHz half wavelength piezoelectric sandwich transducer, and a 25-mm-diameter tip acoustic sonotrode made from Ti-6Al-4V alloy. The maximum vibration amplitude at the sonotrode working face is 12 ± 1 μm peak to peak. The sonotrode was immersed into the melt to a depth of 10 mm at 973 K (700 °C) with the ultrasonic system switched on prior to immersion. The sonotrode was preheated to 773 K (500 °C) before it was immersed into the melt to alleviate the tendency for a solidified layer to form on the sonotrode working face. It was removed from the melt at 883 K (610 °C).

The ultrasonic intensity, I, required to overcome the cavitation threshold in typical Al melts has been determined to be $I \geq 100$ W cm^{-2},[19] where I is defined by[19]

$$I = 0.5\,\rho c(2\pi f A)^2, \qquad [1]$$

where ρ is the liquid mass density, c is the speed of sound in the liquid, f is the frequency, and A is the amplitude of the ultrasound. The density of Al at 973 K (700 °C) (*i.e.*, the USMT start temperature) is 2375 kg m^{-3},[37] which increases to 2395 kg m^{-3} when alloyed with 19 pct Si and 4 pct Fe.[14] The speed of sound in the alloy used is assumed to be that of a simple Al-19 pct Si binary alloy which at 973 K (700 °C) has been reported to be 4573 m s^{-1}.[38] The ultrasonic intensity at the sonotrode working face-melt interface can be estimated to be 1245 W cm^{-2} using Eq. [1], which is over an order of magnitude greater than the ultrasonic intensity threshold (100 W cm^{-2}) required for the formation of a cavitation zone.

C. *Characterization*

As-solidified ingot samples were sectioned longitudinally for metallographic observations. The half castings were cut into small pieces, each with a section area of 10 mm × 10 mm at four different positions on the cross

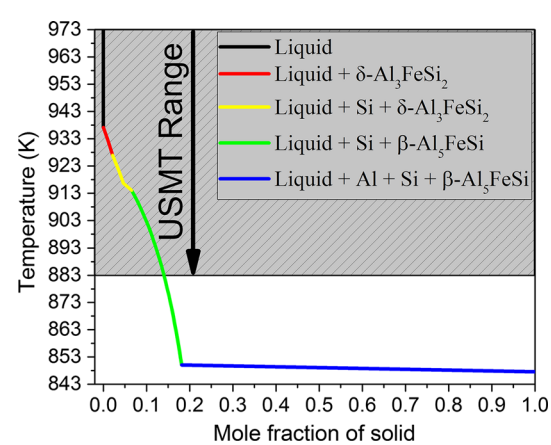

Fig. 2—Temperature *vs* fraction solid curve as predicted by PANDAT™ assuming equilibrium solidification of the Al-19Si-4Fe alloy.

section, representing the top surface, central, bottom, and side wall regions of the casting, as shown in Figure 3. The samples were mounted, ground, and polished, using standard metallographic techniques.

The morphology and composition of phases were examined with an FEI NanoSEM scanning electron microscope (SEM) in the backscattered electron (BSE) mode, equipped with an Oxford Instruments X-MaxN 20 energy dispersive X-ray spectroscopy (EDS) detector. Image analysis software package ImageJ was used to investigate and measure various microstructural parameters of the different phase constituents from the backscattered images. At least 15 fields of view were analyzed for each zone, where each field covered an area of 2.64 mm^2.

III. RESULTS

A. *The Effect of USMT on Cooling Curves*

The Lever rule module of Pandat™[39] with the PanAluminium 2016 database was used for solidification simulation of the Al-19Si-4Fe alloy. Figure 2 presents the temperature *vs* fraction solid of the alloy, in which the following series of reactions take place:

(1) $L \rightarrow \delta\text{-}Al_3FeSi_2$ 937 K (664 °C)
(2) $L \rightarrow \delta\text{-}Al_3FeSi_2 + Si$ 927 K (654 °C)
(3) $L + \delta\text{-}Al_3FeSi_2 \rightarrow \beta\text{-}Al_5FeSi + Si$ 914 K (641 °C)
(4) $L \rightarrow \alpha\text{-}Al + Si + \beta\text{-}Al_5FeSi$ 848 K (575 °C).

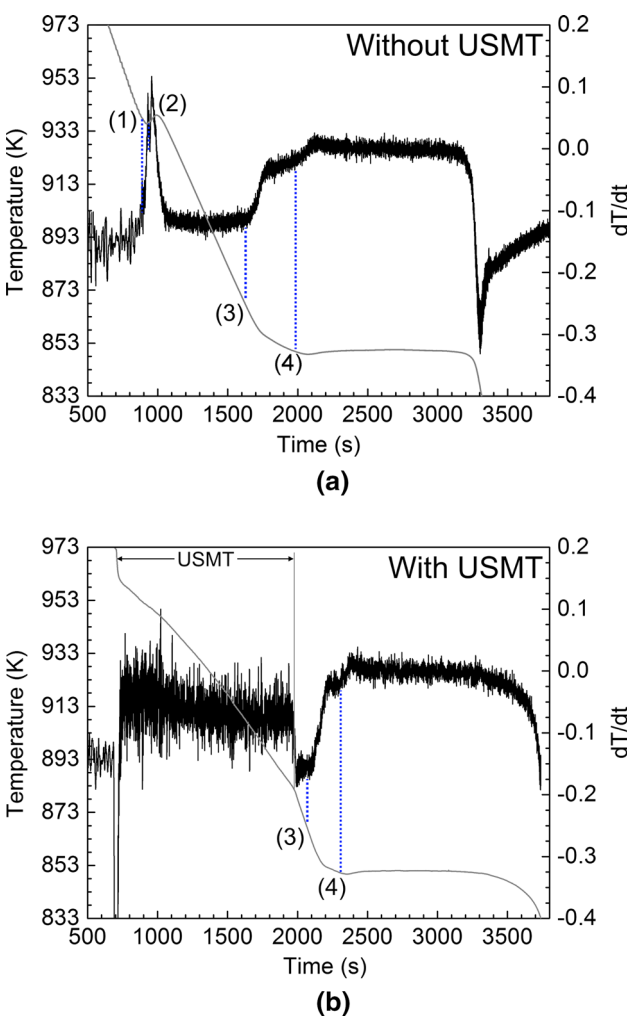

Fig. 3—Cooling curves and their first derivatives for the Al-19Si-4Fe alloy: (*a*) without USMT and (*b*) with USMT.

Figures 3(a) and (b) show the cooling curves and their first derivatives obtained for the alloy without and with USMT. The reaction temperatures were determined from the first derivative.[40] Based on Figure 2, the reaction and corresponding temperatures are listed in Table II.

Solidification of the alloy without USMT starts at 938 K (665 °C), corresponding to the precipitation of $\delta\text{-}Al_3FeSi_2$ (marked 1 in the figure). A second reaction overlaps considerably with the first one given the small temperature difference between these two reactions. Nonetheless, primary Si precipitation occurs at 936 K (663 °C) (marked 2). The peritectic reaction $L + \delta\text{-}Al_3FeSi_2 \rightarrow \beta\text{-}Al_5FeSi + Si$ takes place at 868 K (595 °C) (marked 3). Lastly, the main ternary eutectic reaction $L \rightarrow \alpha\text{-}Al + Si + \beta\text{-}Al_5FeSi$ occurs at 849 K (576 °C) (marked 4). These experimentally determined reaction temperatures are consistent with the thermodynamic predictions, except for the peritectic reaction (3) where the difference between the values is 46 K. Meanwhile, the experimentally observed peritectic reaction temperature of 868 K (595 °C) is consistent with literature data, such as 868 K (595 °C)[41] and 869 K (596 °C).[42]

For the alloy with USMT, the insertion of the sonotrode at 973 K (700 °C) led to a sudden drop in melt temperature of about 12 K, followed by a decrease in cooling rate to a relatively stable rate of ~0.06 K s^{-1}. The sonotrode itself increases the heat extraction rate rapidly, until the point where the temperature of the sonotrode reaches thermal equilibration with the melt and the cooling rate stabilizes afterward. During USMT, there was much more noise in the temperature signal. This is likely related to the cavitation and acoustic streaming effects in the region of the thermocouple tip. As a result, the reaction arrest temperatures for the precipitation of primary $\delta\text{-}Al_3FeSi_2$ and primary Si are difficult to determine. Upon removing the sonotrode at 883 K (610 °C), a sudden increase in the cooling rate occurs to a stable rate of ~0.16 K s^{-1}. The acoustic energy introduced into the melt can effectively lead to a slower cooling rate during treatment.[19] Finally, the peritectic (marked 3) and ternary eutectic (marked 4) reactions occur at 868 K (595 °C) and 849 K (576 °C), which are the same temperatures as without USMT.

B. *The Effect of USMT on the Macrostructure*

Figures 4(a) and (b) present optical macrographs of the vertical sections of the alloy without and with USMT. In the absence of USMT, primary Fe-containing intermetallics and primary Si are concentrated near

Table II. Solidification Reactions Observed from the Cooling Curves of the Al-19Si-4Fe Alloy Without and With USMT

Reaction Number	Type of Reaction	Estimated Temperature, K (°C)	
		Without USMT	With USMT
(1)	$L \rightarrow \delta\text{-}Al_3FeSi_2$	938 (665)	*
(2)	$L \rightarrow \delta\text{-}Al_3FeSi_2 + Si$	936 (663)	*
(3)	$L + \delta\text{-}Al_3FeSi_2 \rightarrow \beta\text{-}Al_5FeSi + Si$	868 (595)	868 (595)
(4)	$L \rightarrow \alpha\text{-}Al + Si + \beta\text{-}Al_5FeSi$	849 (576)	849 (576)

*Difficult to determine from the experimental data (see text).

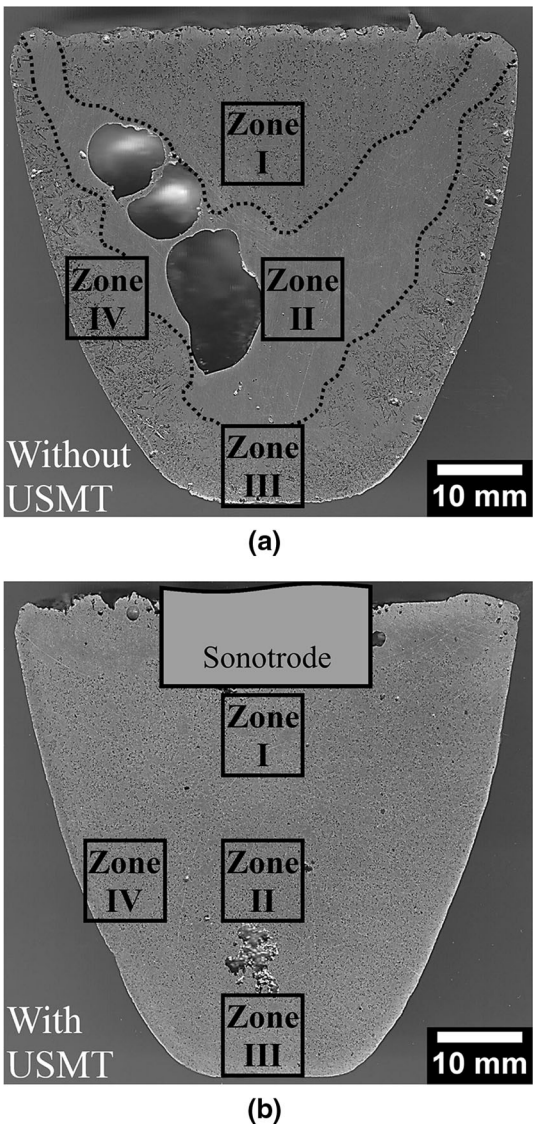

Fig. 4—(*a*) Vertical section of a solidified Al-19Si-4Fe ingot without USMT and (*b*) the same alloy with USMT. Note the distinct difference in macro-segregation and phase distribution in (a) and (b).

the top surface (Zone I in Figure 4(a)) as well as the bottom and side walls of the crucible (Zones III and IV in Figure 4(a)). No primary particles are visible in the central region (Zone II), which covers about 60 vol pct of the ingot. Additionally, large shrinkage cavities appear in the central region. With USMT, these cavities are essentially eliminated, and, at least from a macroscopic point of view, fine Fe-containing intermetallics and primary Si particles are uniformly distributed throughout the ingot.

C. *The Effect of USMT on Microstructure*

Figure 5 shows the morphologies of primary Fe-containing intermetallics (white) and primary Si (gray) revealed by SEM BSE images in different regions of the ingot samples solidified without and with USMT. The main features can be summarized as follows: (i) the long platelet-like primary Fe-containing intermetallics observed in Zone I of the ingot without USMT disappeared after USMT; (ii) after USMT, the morphologies of the primary Fe-containing intermetallics and primary Si particles are observed to be finer and more homogeneous compared to without USMT and display approximately rod-like and polyhedral morphologies, respectively; (iii) both the primary phase particles are well distributed across all zones of the ingot with USMT, as opposed the non-uniform microstructure of the ingot without USMT where primary phase particles are evident near the melt surface and wall regions but are absent in the central region.

D. *Quantitative Microstructural Analysis*

Area fraction provides a useful measure of the distribution of each primary phase in the ingot. Figures 6(a) and (b) show the area fractions of the primary Fe-containing intermetallic and primary Si phases in different regions of the ingots without and with USMT. USMT resulted in both the primary Fe-containing intermetallic and primary Si crystals to be distributed essentially uniformly across the ingot compared to noticeable variations, *i.e.,* macro-segregation, in the absence of USMT.

The number density per unit area of each primary phase in the ingot samples is shown in Figures 7(a) and (b). An appreciable increase in number density was observed after USMT for both the primary Fe-containing intermetallics and primary Si in each region concerned. Equally important is that the number density distribution in the ingot after USMT is far more uniform across all zones of the ingot than in the absence of USMT.

Along with significant changes in distribution are modified shapes of each primary phase. Figures 8(a) through (d) show the measured morphological parameters of each primary phase from different regions of the

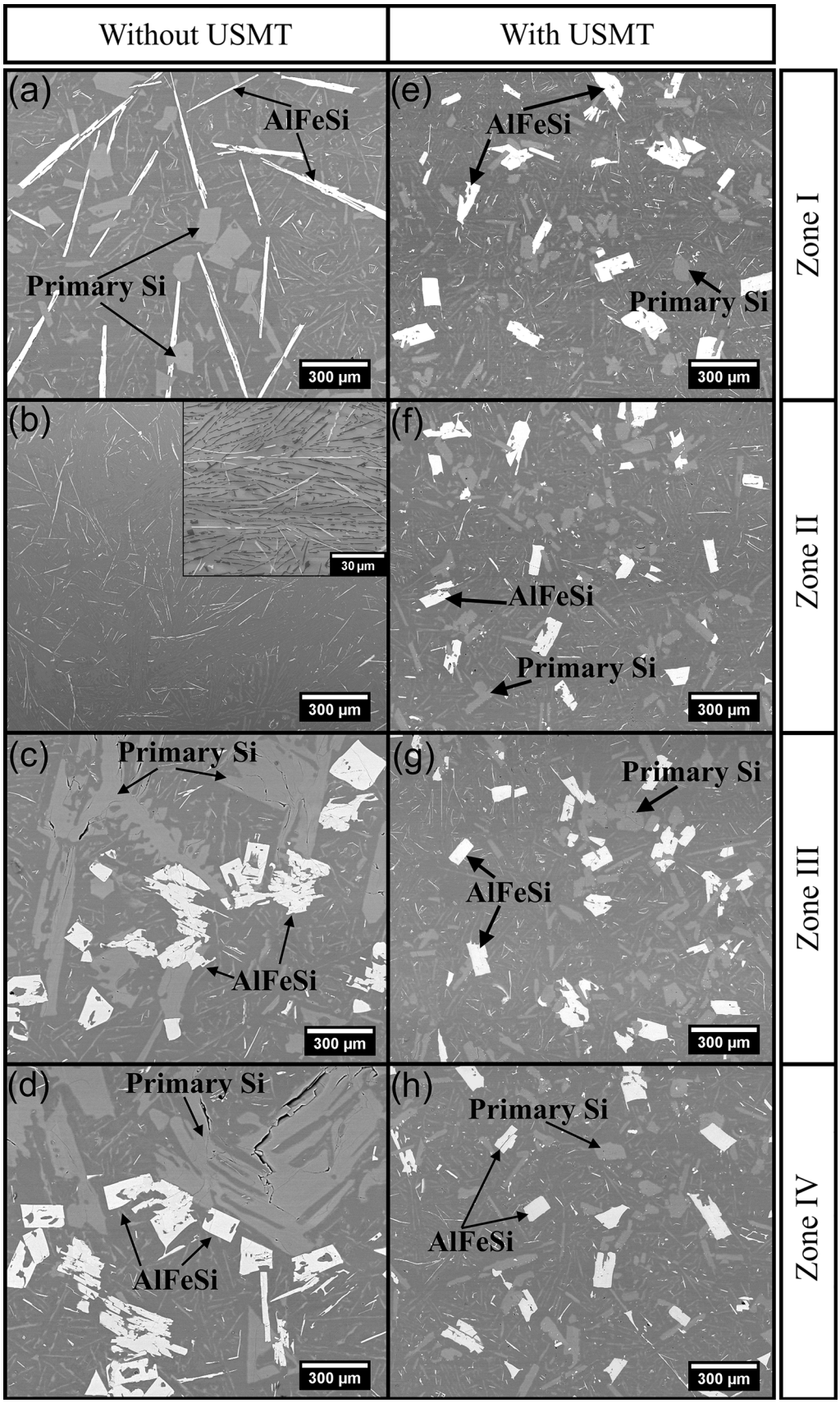

Fig. 5—SEM BSE micrographs showing the typical primary phase structures in the four different zones of the Al-19Si-4Fe ingots shown in Fig. 4.

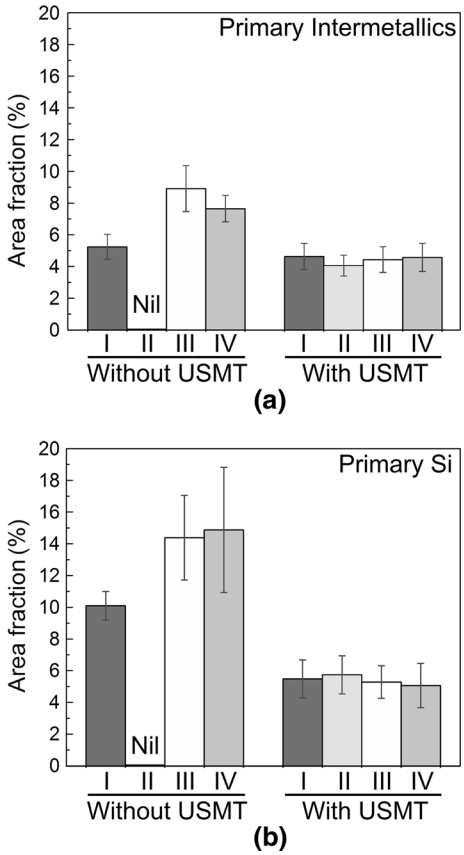

Fig. 6—Area fraction of primary phases without and with USMT in the ingot samples shown in Fig. 4: (*a*) primary Fe-containing intermetallics, and (*b*) primary Si. Refer to Fig. 4 for the different zones.

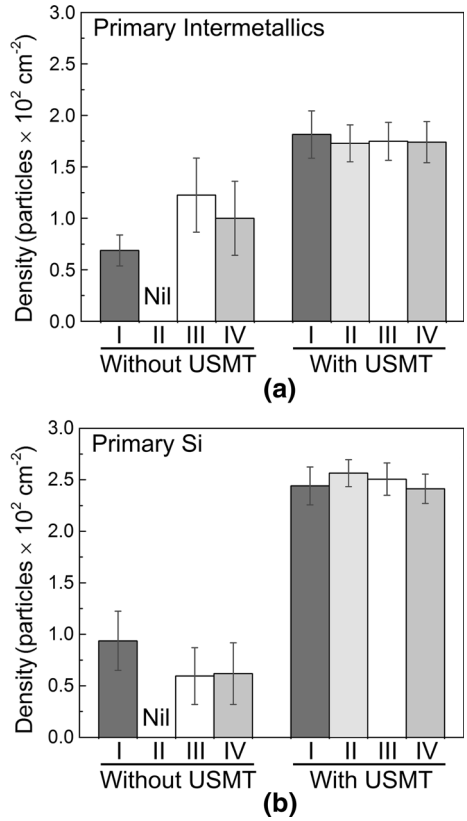

Fig. 7—Number density of primary phases without and with USMT for the ingot samples shown in Fig. 4: (*a*) primary Fe-containing intermetallics, and (*b*) primary Si. Refer to Fig. 4 for the different zones.

ingot samples shown in Figure 4. USMT entailed a marked reduction in both the length and width of each primary phase. Also, the size is more homogeneous throughout the ingot after USMT, while the difference in size is considerable without USMT.

E. *Complex Particles of δ-Al_3FeSi_2/β-Al_5FeSi*

A closer inspection of the backscattered micrographs revealed that many of the primary Fe-containing intermetallics existed in a complex form which contained a central lighter phase enveloped by a darker phase in the ingot sample solidified without USMT. In contrast, such particles were observed only occasionally in the ingot sample solidified with USMT. In fact, the vast majority of the primary Fe-containing intermetallic particles in the ingot sample after USMT appeared as single-phase particles.

Figure 9 shows a representative BSE image of two coarse platelet-like complex primary Fe-containing intermetallic particles observed in Zone I of the ingot sample solidified without USMT. The faint difference in contrast can easily mask the two different intermetallic phases at low magnifications. Figures 10(a) through (c) show typical blocky complex primary Fe-containing intermetallic particles observed near the wall of the ingot sample without USMT. The relative volume fraction of each phase in the complex particle varies but in all of the complex particles observed the central lighter contrast intermetallic phase showed a large area fraction. For comparison, Figures 10(d) and (e) show two examples of the single-phase Fe-containing intermetallic particles that are predominant in the ingot sample after USMT. Only a few complex particles were encountered in the ingot sample after USMT. A useful feature to note is that the central lighter contrast intermetallic phase is much smaller than those observed in the case without USMT. Figure 10(f) shows one such example. It would appear that the central particle is the remnant of a larger particle formed at the beginning of solidification.

EDS line scan analyses along the cross section of each selected intermetallic particle from Figure 10 are shown in Figure 11. The results confirm that the contrasting phases in the complex particles are not artifacts. Instead, the central phase contained more Si than the outer phase (Figure 11(a, b)). The single-phase particles shown in Figure 10(f) do not contain an inner Si-rich phase (Figure 11(c)). A comprehensive quantitative survey of the chemical compositions of a total of 93 complex and single-phase intermetallic particles was undertaken, and the results are summarized in Table III. Based on these results, the stoichiometry of the central Si-enriched phase is consistent with δ-Al_3FeSi_2, while the outer phase corresponds to β-Al_5FeSi. The stoichiometry of the single-phase short rod particles is consistent with β-Al_5FeSi.

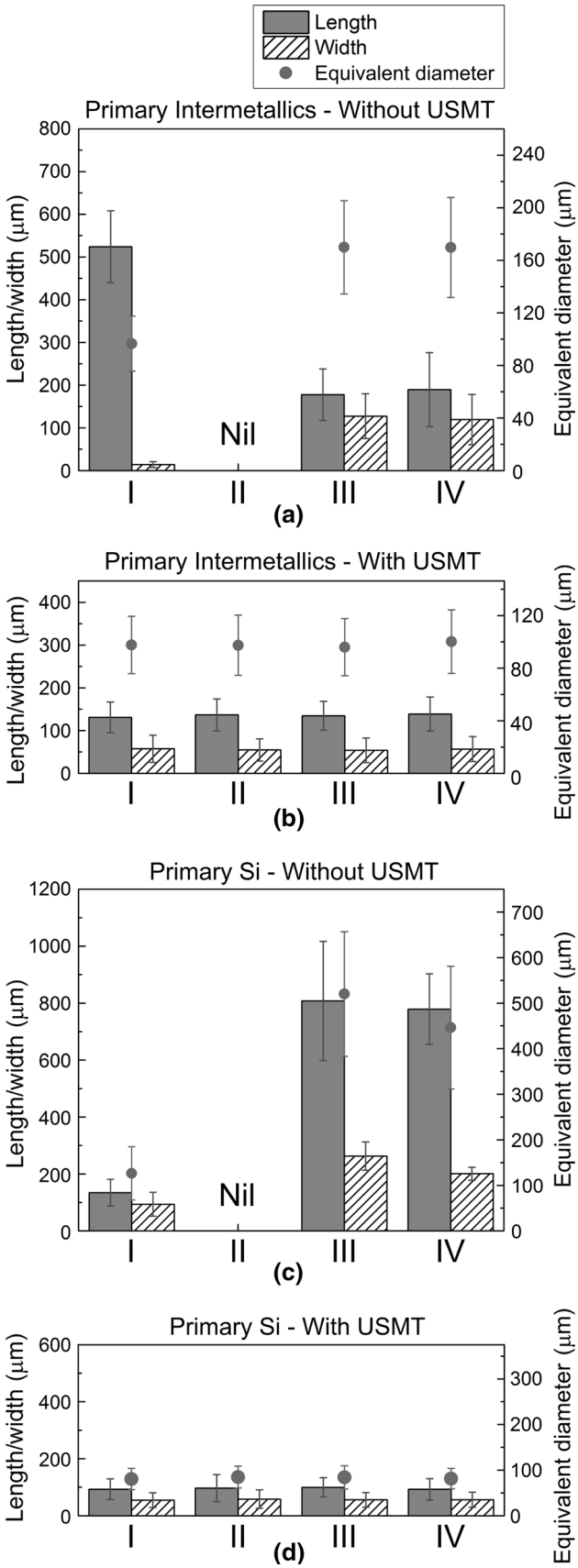

◀Fig. 8—Morphological parameters of primary phases for the alloy ingots shown in Fig. 4: (*a*) primary Fe-containing intermetallics without USMT; (*b*) primary Fe-containing intermetallics with USMT; (*c*) primary Si without USMT; and (*d*) primary Si with USMT. Refer to Fig. 4 for the different zones.

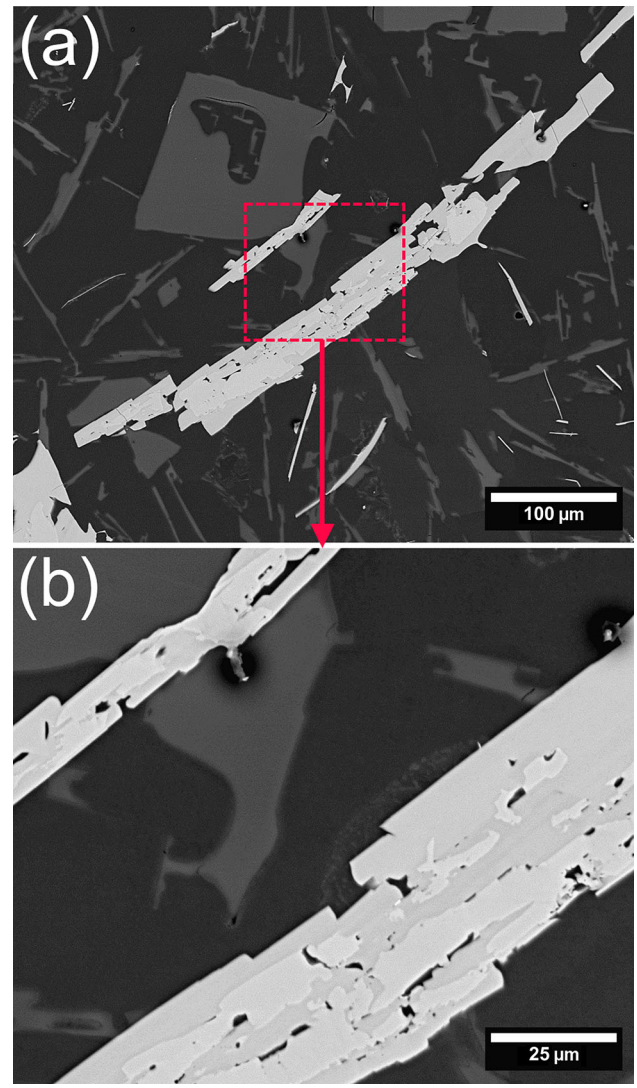

Fig. 9—(*a*) Typical BSE image showing unreacted platelet-like Fe-containing intermetallics existing as complex particles of δ-Al_3FeSi_2/β-Al_5FeSi in Zone I of the ingot sample solidified without USMT, and (*b*) an enlarged view.

IV. DISCUSSION

A. *The Effect of USMT on Macro-Segregation*

The occurrence of macro-segregation of primary Fe-containing intermetallics and primary Si was not unexpected based on previous studies.[43,44] The main mechanisms for the macro-segregation of primary Si particles have been identified as including[32] (i) flotation of primary Si particles toward the top of the melt; (ii)

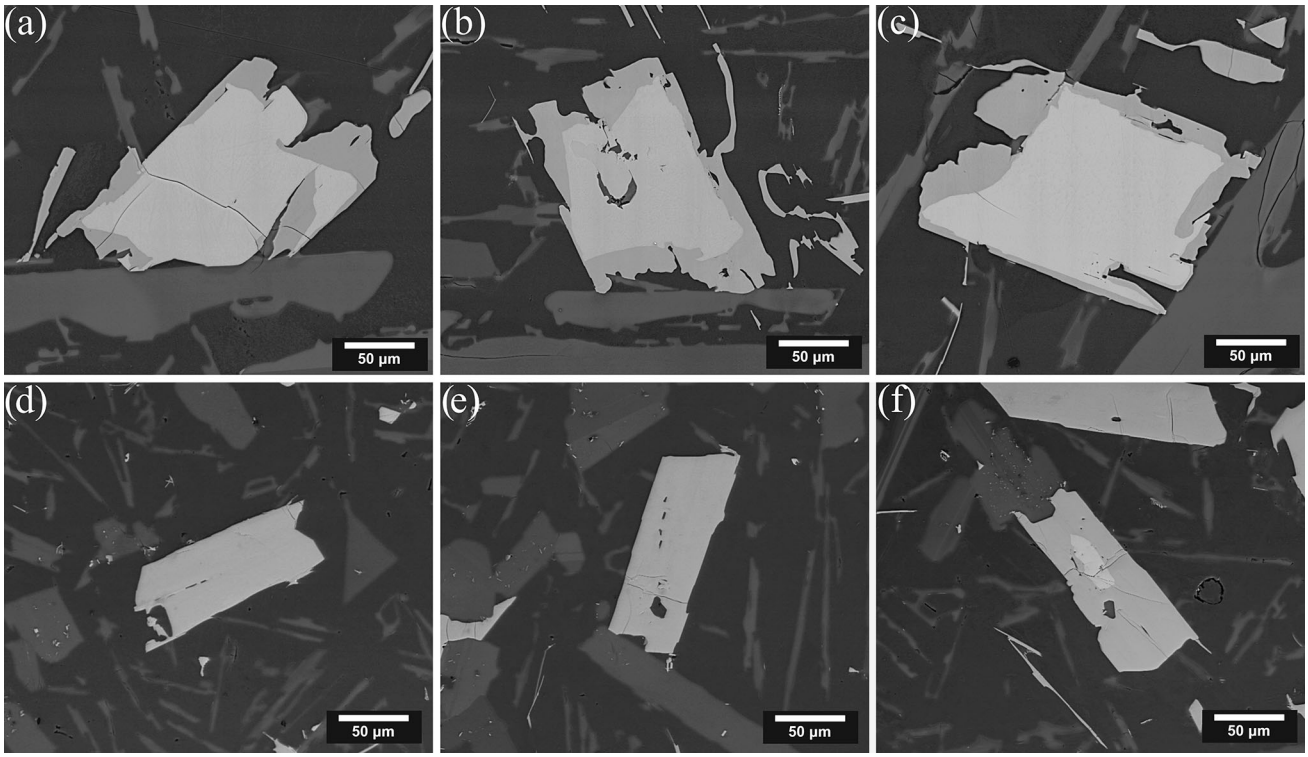

Fig. 10—BSE images showing examples of primary Fe-containing intermetallic particles: (*a* through *c*) complex blocky particles of δ-Al_3FeSi_2/β-Al_5FeSi observed near the mold wall regions of the ingot samples solidified without USMT; (*d*, *e*) single-phase short intermetallic particles observed in the ingot after USMT; and (*f*) a complex particle of δ-Al_3FeSi_2/β-Al_5FeSi observed in the ingot sample with USMT.

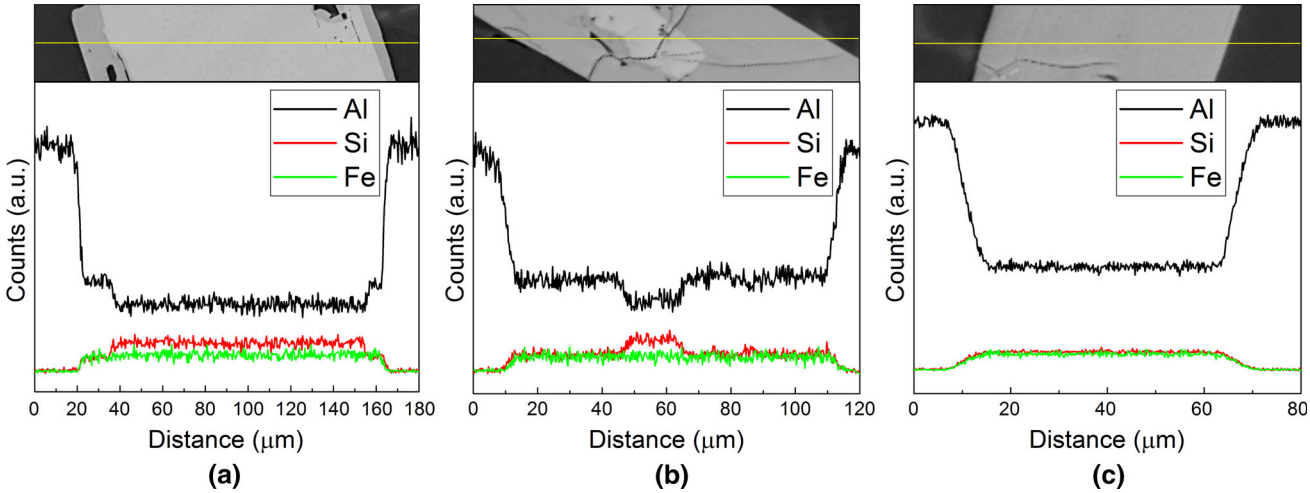

Fig. 11—EDS line scans across selected Fe-containing intermetallics particles: (*a*) the complex particle in Fig. 9(c); (*b*) the complex particle in Fig. 9(f); and (*c*) the single-phase β-Al_5FeSi particle in Fig. 9(e).

Table III. EDS Point Analysis Results of Primary Fe-Containing Intermetallic Particles

			Composition (At. Pct)				
Alloy	Structure		Al	Fe	Si	Fe:Si	Probable Phase
Without USMT	complex particles	central	50.92 ± 3.28	18.03 ± 3.11	31.05 ± 0.84	0.58 ± 0.07	δ-Al_3FeSi_2
		outer	65.89 ± 0.77	16.47 ± 0.88	17.64 ± 0.93	0.92 ± 0.10	β-Al_5FeSi
With USMT	single-phase particles	—	65.94 ± 0.77	16.30 ± 0.67	17.76 ± 0.57	0.92 ± 0.05	β-Al_5FeSi
	complex particles	central	50.97 ± 4.62	18.19 ± 4.06	30.85 ± 0.83	0.59 ± 0.09	δ-Al_3FeSi_2
		outer	65.96 ± 1.17	16.53 ± 0.92	17.51 ± 0.87	0.94 ± 0.10	β-Al_5FeSi

heterogeneous nucleation of primary Si on the mold wall; and (iii) localized enhanced growth of primary Si particles. As regards the macro-segregation of primary Fe-containing intermetallics in Al alloys, they are observed to frequently settle to the bottom of the mold due to gravity leaving the upper part of the casting or ingot depleted of intermetallics.[44] It has also been proposed that some Fe-containing intermetallics may not settle but instead "hang" near both the side mold wall and the top melt surface regions.[44] One possible reason is due to heterogeneous nucleation of primary Fe-containing intermetallics on oxide films or the mold wall, which can effectively slow down or even prevent their sedimentation. This hypothesis can help to explain the macro-segregation of primary phase particles observed near the top melt surface and wall regions, and also their depletion in the central region of the casting. Nonetheless, the mechanisms remain incompletely identified.

USMT produced a uniform distribution of both primary Fe-containing intermetallics and primary Si (Figure 6) and eliminated macro-segregation. In addition, it increased the number of each primary phase (Figure 7) with a uniform size distribution (Figure 8). The high potency of USMT in dispersing the primary Fe-containing intermetallics and primary Si can be attributed to the combined effects of the enhanced heterogeneous nucleation of each primary phase (cavitation-induced, including fragmentation) and dynamic solidification environment (acoustic streaming and cavitation) created by ultrasonic waves. Both effects of USMT have long been recognized and discussed in the literature.[18–23,45] They will not be restated herein. One additional benefit of the cavitation effect of USMT is that it produces an essentially thoroughly mixed effect, thereby preventing large primary phase particles from quickly sinking or floating. As a result, gravity segregation of the primary phase particles is mitigated. This ability of USMT to fully eliminate macro-segregation so efficiently has not been well demonstrated previously to the authors' best knowledge and it was not totally expected prior to this research. In that regard, this research extends perspectives on the capabilities of USMT.

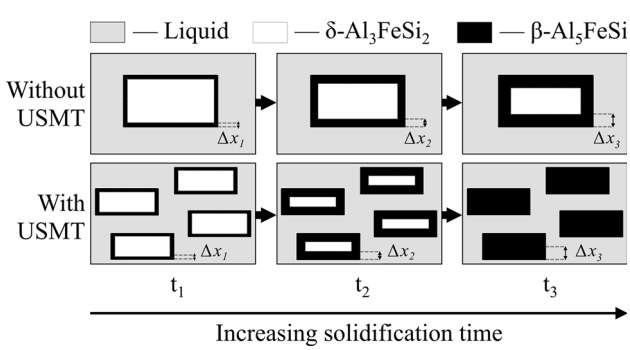

Fig. 12—Schematic diagram showing the effect of USMT on the peritectic transformation δ-$Al_3FeSi_2 \rightarrow \beta$-$Al_5FeSi$. The finer primary δ-Al_3FeSi_2 particles produced as a result of USMT ensure their complete transformation into peritectic β-Al_5FeSi phase.

B. *The Effect of USMT on Peritectic Transformation of Intermetallics*

The thermodynamic calculation shown in Figure 2 predicts that an invariant quasi-peritectic reaction L + δ-$Al_3FeSi_2 \rightarrow \beta$-$Al_5FeSi$ + Si occurs during solidification of the Al-19Si-4Fe alloy. As proposed by Sha *et al.*,[17] the study of quasi-peritectic reactions can be based on the normal peritectic reaction theory.[46–52] On this basis, the quasi-peritectic formation of β-Al_5FeSi can be regarded as consisting of two stages: (i) the normal peritectic reaction, during which direct reaction between δ-Al_3FeSi_2 and liquid leads to the formation of a continuous envelope of β-Al_5FeSi surrounding each δ-Al_3FeSi_2 particle, isolating the initial δ-Al_3FeSi_2 phase from further contacting liquid; and (ii) the peritectic transformation, during which the β-Al_5FeSi envelope thickens by solid-state diffusion of alloying elements from δ-Al_3FeSi_2 and liquid phases through the peritectic β-Al_5FeSi envelope. It has been reported that both the δ-Al_3FeSi_2 and β-Al_5FeSi particles exhibit similar platelet-like characteristic crystal shapes, but the platelets of δ-Al_3FeSi_2 are generally more blocky.[53] Hence, if the transformation from δ-Al_3FeSi_2 into β-Al_5FeSi goes to completion, only relatively thin platelet-like β-Al_5FeSi particles will appear in the as-solidified microstructure. However, if the transformation is only partially complete, both δ-Al_3FeSi_2 and β-Al_5FeSi will be present as complex particles exhibiting an intermediary blocky-to-platelet morphology in which β-Al_5FeSi envelopes δ-Al_3FeSi_2. In general, under most cooling conditions during solidification, only fine δ-Al_3FeSi_2 particles are expected to undergo complete transformation into β-Al_5FeSi as the transformation is slow due to solid-state diffusion.

In the ingot sample solidified without USMT, the primary Fe-containing intermetallics exhibited long platelet-like shapes (Figure 5(a)) in the melt surface (Zone I) and blocky shapes (Figures 5(c, d)) in the wall regions (Zones III and IV). They both formed as complex particles of δ-Al_3FeSi_2/β-Al_5FeSi. However, the blocky particles contained a significantly larger δ-Al_3FeSi_2 particle than those in the melt surface region. We propose that this is due to different degrees of transformation of δ-Al_3FeSi_2 into β-Al_5FeSi.

Table IV. The Average Intermetallic Half-Width (Critical Diffusion Length) and the Average Thickness of the Peritectic β-Al_5FeSi Phase Envelope in the Alloy Without and With USMT

Alloy	Half-Width of the Particle (μm)	Thickness of the Peritectic Envelope (μm)
Without USMT	61.6 ± 20.7	24.6 ± 15.4
With USMT	27.7 ± 6.9	26.4 ± 5.7

Figure 8(a) shows that the average equivalent size of the primary Fe-containing intermetallic particles formed near the mold wall regions are almost twice as large as those formed near the melt surface regions. The diffusion-controlled rate of transformation from δ-Al_3FeSi_2 to β-Al_5FeSi can be assumed to be similar at the same temperature. Therefore, the less complete transformation of δ-Al_3FeSi_2 into β-Al_5FeSi platelets observed at the mold wall regions versus that at the melt surface can be attributed to the existence of coarser particles of δ-Al_3FeSi_2 for which longer time is required to complete the peritectic transformation.

After USMT, most primary Fe-containing intermetallics exist as single-phase β-Al_5FeSi short rod particles (Figures 10(d through e)) with a few δ-Al_3FeSi_2/β-Al_5FeSi complex particles containing a small central area of primary δ-Al_3FeSi_2 (Figure 10(f)). USMT has clearly resulted in complete peritectic transformation of most primary δ-Al_3FeSi_2 particles into peritectic β-Al_5FeSi. As shown schematically in Figure 12, the finer sized primary δ-Al_3FeSi_2 particles will shorten the time needed to complete the peritectic transformation. USMT produced much finer δ-Al_3FeSi_2 particles thus reducing the time needed to achieve complete transformation to β-Al_5FeSi. In addition, USMT may have further enhanced the peritectic transformation by accelerating the peritectic transformation rate, in which case the thickness of the peritectic envelope $\Delta\beta$-Al_5FeSi in the alloy after USMT would be greater than that in the case without USMT. Previous studies[32–34] have suggested that the peritectic transformation rate increases markedly under USMT, possible due to two mechanisms: (1) acceleration of the liquid-peritectic phase interfacial diffusion due to cavitation and accompanied mixing of the melt; and (2) increase in the peritectic reaction temperature according to the Clapeyron equation,[54] and thus diffusion is expected to increase with temperature. To clarify this point, the β-Al_5FeSi envelope thicknesses were measured for at least 40 particles in both alloys, and the results are shown in Table IV. An average envelope thickness of 24.6 μm was achieved without USMT, as opposed to 26.4 μm with USMT. The very similar values indicate that the rate of peritectic transformation δ-$Al_3FeSi_2 \rightarrow \beta$-$Al_5FeSi$ remained essentially the same in both alloys. This is not totally unexpected since USMT ceased prior to the peritectic reaction as shown in Figure 3(b). Consequently, the observations of ultrasound enhancing the peritectic transformation are mainly due to the reduced size of the primary δ-Al_3FeSi_2 particles which require much less time to complete transformation than larger primary δ-Al_3FeSi_2 phase particles.

V. CONCLUSIONS

1. In the absence of ultrasonic melt treatment (USMT), severe macro-segregation was observed in the ingot with a noticeably non-uniform distribution of primary Fe-containing intermetallic and primary Si particles, whereas a near homogeneous distribution of both primary phase particles throughout the ingot was produced after USMT, *i.e.,* reduced macro-segregation.
2. Macro-segregation was further quantified using microstructural metallography at different regions of the ingot samples. The results showed that the area fraction, number density, and size distribution of both the primary Fe-containing intermetallic and primary Si particles became essentially uniform across the ingot after USMT confirming the beneficial effect of USMT on eliminating macro-segregation.
3. USMT had a significant impact on the constitution of the primary Fe-containing intermetallics, where complex particles of δ-Al_3FeSi_2/β-Al_5FeSi were prominent without USMT, while few δ-Al_3FeSi_2 particles were observed after USMT and the primary Fe-containing intermetallics existed mostly as the single-phase β-Al_5FeSi.
4. USMT leads to enhanced peritectic transformation δ-$Al_3FeSi_2 \rightarrow \beta$-$Al_5FeSi$ due to the significant reduction in the average size of the primary δ-Al_3FeSi_2 particles.

ACKNOWLEDGMENTS

The project was funded by the Australian Research Council (ARC) through DP140100702. Collaboration through the ExoMet Project co-funded by the European Commission's 7th Framework Programme (Contract FP7-NMP3-LA-2012-280421), by the European Space Agency, and by the individual partner organizations, is acknowledged. We also express our appreciation to Mr. G. Savage, Mr. A. Yob, Mr. J. Read, Mr. D. Graham, and Mr. S. Djordjevic for their assistance with experimental work. We acknowledge the facilities, and the scientific and technical assistance, of the Australian Microscopy & Microanalysis Research Facility at RMIT University.

REFERENCES

1. J. Zhou, J. Duszczyk, and B.M. Korevaar: *J. Mater. Sci.*, 1991, vol. 26, pp. 3041–50.
2. T.S. Kim, C. Suryanarayana, and B.S. Chun: *Mater. Sci. Eng. A*, 2000, vol. 278, pp. 113–20.
3. L. Wang, M. Makhlouf, and D. Apelian: *Int. Mater. Rev.*, 1995, vol. 40, pp. 221–38.
4. N. Tenekedjiev, D. Argo, and J.E. Gruzleski: *AFS Trans.*, 1989, vol. 97, pp. 127–36.
5. M. Rajabi, M. Vahidi, A. Simchi, and P. Davami: *Mater. Charact.*, 2009, vol. 60, pp. 1370–81.
6. H.J. Huang, Y.H. Cai, H. Cui, J.F. Huang, J.P. He, and J.S. Zhang: *Mater. Sci. Eng. A*, 2009, vol. 502, pp. 118–25.
7. Q.L. Wang, H.R. Geng, S. Zhang, H.W. Jiang, and M. Zuo: *Metall. Mater. Trans. A*, 2014, vol. 45A, pp. 1621–30.
8. Y. Osawa, S. Takarnori, T. Kimura, K. Minagawa, and H. Kakisawa: *Mater. Trans.*, 2007, vol. 48, pp. 2467–75.
9. G. Zhong, S.S. Wu, H.W. Jiang, and P. An: *J. Alloy. Compd.*, 2010, vol. 492, pp. 482–87.
10. M. Sha, S.S. Wu, and L. Wan: *Mater. Sci. Eng. A*, 2012, vol. 554, pp. 142–48.

11. C. Lin, S.S. Wu, S.L. Lu, and P. An: *J. Alloy. Compd.*, 2013, vol. 568, pp. 42–48.
12. C. Lin, S.S. Wu, S.L. Lu, P. An, and L. Wan: *Intermetallics*, 2013, vol. 32, pp. 176–83.
13. W. Khalifa, S. El-Hadad, and Y. Tsunekawa: *Metall. Mater. Trans. A*, 2013, vol. 44A, pp. 5817–24.
14. L.F. Mondolfo: *Aluminum Alloys: Structure and Properties*, Butterworths, London, 1976.
15. W. Khalifa, F.H. Samuel, and J.E. Gruzleski: *Metall. Mater. Trans. A*, 2003, vol. 34A, pp. 807–25.
16. M.H. Mulazimoglu, A. Zaluska, J.E. Gruzleski, and F. Paray: *Metall. Mater. Trans. A*, 1996, vol. 27A, pp. 929–36.
17. G. Sha, K.A.Q. O'Reilly, B. Cantor, J.M. Titchmarsh, and R.G. Hamerton: *Acta Mater.*, 2003, vol. 51, pp. 1883–97.
18. O.V. Abramov: *Ultrasound in liquid and solid metals*, CRC Press, Boca Raton, FL, 1994.
19. G.I. Eskin and D.G. Eskin: *Ultrasonic Treatment of Light Alloy Melts*, 2nd ed., CRC Press, Boca Raton, FL, 2014.
20. A. Ramirez, M. Qian, B. Davis, T. Wilks, and D.H. StJohn: *Scr. Mater.*, 2008, vol. 59, pp. 19–22.
21. M. Qian, A. Ramirez, and A. Das: *J. Cryst. Growth*, 2009, vol. 311, pp. 3708–15.
22. M. Qian, A. Ramirez, A. Das, and D.H. StJohn: *J. Cryst. Growth*, 2010, vol. 312, pp. 2267–72.
23. T.V. Atamanenko, D.G. Eskin, L. Zhang, and L. Katgerman: *Metall. Mater. Trans. A*, 2010, vol. 41A, pp. 2056–66.
24. G. Wang, M.S. Dargusch, M. Qian, D.G. Eskin, and D.H. StJohn: *J. Cryst. Growth*, 2014, vol. 408, pp. 119–24.
25. N. Srivastava, G.P. Chaudhari, and M. Qian: *J. Mater. Process. Technol.*, 2017, vol. 249, pp. 367–78.
26. H.R. Kotadia, M. Qian, D.G. Eskin, and A. Das: *Mater. Design*, 2017, vol. 132, pp. 266–74.
27. W. Khalifa, Y. Tsunekawa, and M. Okumiya: *J. Mater. Process. Technol.*, 2010, vol. 210, pp. 2178–87.
28. V.O. Abramov, O.V. Abramov, B.B. Straumal, and W. Gust: *Mater. Des.*, 1997, vol. 18, pp. 323–26.
29. G.I. Eskin and D.G. Eskin: *Ultrason. Sonochem.*, 2003, vol. 10, pp. 297–301.
30. H.K. Feng, S.R. Yu, Y.L. Li, and L.Y. Gong: *J. Mater. Process. Technol.*, 2008, vol. 208, pp. 330–35.
31. J.B. Ferguson, M. Tabandeh-Khorshid, J.C. Mantas, P.K. Rohatgi, K. Cho, and C.S. Kim: *Metall. Mater. Trans. B*, 2014, vol. 45B, pp. 1407–17.
32. W. Zhai and B.B. Wei: *Mater. Lett.*, 2015, vol. 138, pp. 1–4.
33. W. Zhai, Z.Y. Hong, X.L. Wen, D.L. Geng, and B. Wei: *Mater. Des.*, 2015, vol. 72, pp. 43–50.
34. R. Chen, D. Zheng, T. Ma, H. Ding, Y. Su, J. Guo, and H. Fu: *Ultrason. Sonochem.*, 2017, vol. 38, pp. 120–33.
35. H.R. Kotadia, A. Das, E. Doernberg, and R. Schmid-Fetzer: *Mater. Chem. Phys.*, 2011, vol. 131, pp. 241–49.
36. W. Zhai, H.M. Liu, and B. Wei: *Mater. Lett.*, 2015, vol. 141, pp. 221–24.
37. E.A. Brandes and G.B. Brook: *Smithells Metals Reference Book*, 7th ed., Butterworth-Heinemann, Oxford, 1992.
38. N.M. Keita and S. Steinemann: *J. Phys. C.*, 1978, vol. 11, pp. 4635–41.
39. W. Cao, S.L. Chen, F. Zhang, K. Wu, Y. Yang, Y.A. Chang, R. Schmid-Fetzer, and W.A. Oates: *CALPHAD*, 2009, vol. 33, pp. 328–42.
40. L. Backerud, G. Chai, and J. Tamminen: *Solidification Characteristics of Aluminium Alloys: Foundry Alloys*, AFS/Skanaluminium, Des Plaines, 1990, vol. 2.
41. A.G.C. Gwyer and H.W.L. Phillips: *J. Inst. Met.*, 1927, vol. 38, pp. 29–83.
42. N. Krendelsberger, F. Weitzer, and J.C. Schuster: *Metall. Mater. Trans. A*, 2007, vol. 38A, pp. 1681–91.
43. D. Liang, Y. Bayraktar, S.A. Moir, M. Barkhudarov, and H. Jones: *Scr. Metall. Mater.*, 1994, vol. 31, pp. 363–67.
44. X. Cao, N. Saunders, and J. Campbell: *J. Mater. Sci.*, 2004, vol. 39, pp. 2303–14.
45. F. Wang, D. Eskin, J.W. Mi, T. Connolley, J. Lindsay, and M. Mounib: *Acta Mater.*, 2016, vol. 116, pp. 354–63.
46. H.W. Kerr, J. Cisse, and G.F. Bolling: *Acta Metall.*, 1974, vol. 22, pp. 677–86.
47. A.P. Titchener and J.A. Spittle: *Met. Sci.*, 1974, vol. 8, pp. 112–16.
48. D.H. StJohn and L.M. Hogan: *Acta Metall.*, 1977, vol. 25, pp. 77–81.
49. M. Hillert: *Solidification and Casting of Metals*, The Metals Society, London, 1979, pp. 81–87.
50. H. Fredriksson and T. Nylen: *Met. Sci.*, 1982, vol. 16, pp. 283–94.
51. D.H. StJohn and L.M. Hogan: *Acta Metall.*, 1987, vol. 35, pp. 171–74.
52. D.H. StJohn: *Acta Metall. Mater.*, 1990, vol. 38, pp. 631–36.
53. G. Phragmen: *J. Inst. Met.*, 1950, vol. 77, pp. 489–551.
54. J.D. Hunt: *J. Appl. Phys.*, 1966, vol. 37, pp. 254–57.